

Nowcasting of DNI maps for the solar field based on voxel carving and individual 3D cloud objects from all sky images

Bijan Nouri, Pascal Kuhn, Stefan Wilbert, Christoph Prah, Robert Pitz-Paal, Philippe Blanc, Thomas Schmidt, Zeyad Yasser, Lourdes Ramirez Santigosa, and Detlev Heineman

Citation: [AIP Conference Proceedings](#) **2033**, 190011 (2018); doi: 10.1063/1.5067196

View online: <https://doi.org/10.1063/1.5067196>

View Table of Contents: <http://aip.scitation.org/toc/apc/2033/1>

Published by the [American Institute of Physics](#)

Articles you may be interested in

[Sunshape measurements with conventional rotating shadowband irradiometers](#)

AIP Conference Proceedings **2033**, 190016 (2018); 10.1063/1.5067201

[Model-based soiling estimation in parabolic solar concentrators](#)

AIP Conference Proceedings **2033**, 030018 (2018); 10.1063/1.5067034

[Validation of spatially resolved all sky imager derived DNI nowcasts](#)

AIP Conference Proceedings **1850**, 140014 (2017); 10.1063/1.4984522

[Towards the Chilean solar thermal potential knowledge for solar power tower plants](#)

AIP Conference Proceedings **2033**, 170008 (2018); 10.1063/1.5067172

[Sunbelt spectra comparison with standard ASTM G173: The Chilean case](#)

AIP Conference Proceedings **2033**, 190010 (2018); 10.1063/1.5067195

AIP | Conference Proceedings

Get **30% off** all
print proceedings!

Enter Promotion Code **PDF30** at checkout



Nowcasting of DNI Maps for the Solar Field Based on Voxel Carving and Individual 3D Cloud Objects from All Sky Images

Bijan Nouri^{1, a)}, Pascal Kuhn¹, Stefan Wilbert¹, Christoph Prah¹,
Robert Pitz-Paal², Philippe Blanc³, Thomas Schmidt⁴, Zeyad Yasser⁵,
Lourdes Ramirez Santigosa⁶, Detlev Heineman⁷

¹ DLR, Institute of Solar Research, Plataforma Solar de Almería, Ctra. de Senés s/n km 5, 04200 Tabernas, Spain

² DLR, Institute of Solar Research, Linder Höhe, 51147 Cologne, Germany

³ MINES ParisTech, 06904 Sophia Antipolis CEDEX, France

⁴ CSP Services GmbH, Friedrich-Ebert-Ufer 30, 51143 Cologne, Germany

⁵ TSK Flagsol Engineering GmbH, Anna-Schneider-Steig 10, 50678 Cologne, Germany

⁶ CIEMAT Energy Department – Renewable Energy Division, Av. Complutense 40, 28040 Madrid, Spain

⁷ Universität Oldenburg., Institute of Physics, 26111 Oldenburg, Germany

^{a)} bijan.nouri@dlr.de

Abstract. Accurate nowcasts of the direct normal irradiance (DNI) for the next 15 min ahead can enhance the overall efficiency of concentrating solar power (CSP) plants. Such predictions can be derived from ground based all sky imagers (ASI). The main challenge for existing ASI based nowcasting systems is to provide spatially distributed solar irradiance information for the near future, which considers clouds with varying optical properties distributed over multiple heights. In this work, a novel object oriented approach with four spatially distributed ASIs is presented. One major novelty of the system is the application of an individual 3D model of each detected cloud as a cloud object with distinct attributes (height, position, surface area, volume, transmittance, motion vector etc.). Frequent but complex multilayer cloud movements are taken into account by tracking each cloud object separately. An extended validation period at the Plataforma Solar de Almería (PSA) on 30 days showing diverse weather conditions resulted in an average relative mean absolute error (relMAE) of around 15 % for a medium lead time of 7.5 minutes and a temporal average of 15 minutes. Further reductions of the relMAE were achieved by spatial aggregation, with a relMAE of 10.7 % for a lead time of 7.5 minutes, a field size of 4 km² and a temporal average of 1 minute (during one day). Nowcasting systems described in the literature reach similar deviations but were often validated only for a few days based on a single ground measurement station, which confirms the good performance and the high applicability of the presented system. Three implementations of the system exist already demonstrating the market maturity of the system.

INTRODUCTION

The short-term variability of the Direct Normal Irradiance (DNI) is relevant for Concentrating Solar Power (CSP) plants and originates mainly from transient clouds. Optimized operations of CSP plants require nowcasting tools for various lead times. Several groups have presented cloud detection and nowcasting methods based on one all sky imager (ASI) [1, 2]. However, these methods are not capable of describing complicated multilayer conditions, due to the limited 2D view from a single ASI. Other publications describe methods based on several ASIs which derive 2D cloud layers in up to four different heights [3, 4]. In this work, a novel object oriented approach with four spatially distributed ASIs is presented. The system is currently implemented and operational at the Plataforma Solar de Almería (PSA), the La Africana 50 MWe parabolic trough power plant and the Evora Molten Salt Platform (EMSP). It consists mainly of four standard Mobotix Q24/Q25 surveillance cameras and a

conventional computer which controls the cameras and processes the images. The system also uses DNI measurements, which is part of the standard instrumentation of a CSP plant. Data transmission via a wireless LAN system and optional PV power supply for the cameras enable a quick, flexible and modular installation of the system. New sets of images of all four ASIs are taken simultaneously every 30 s with a resolution of up to 6 MP. The data processing consists of four main tasks: cloud detection, 3D cloud modelling, cloud tracking and the creation of irradiance maps. All tasks, including the preparation of the results for the graphical user interface, are carried out within 30 s. In this paper we describe each task of the system with a focus on the 3D cloud modelling. Later the validation results and a conclusion are presented.

CLOUD OBJECT ORIENTED NOWCASTING SYSTEM

The first step of the nowcasting algorithm is the cloud segmentation. For this purpose a novel four-dimensional clear sky library (CSL) based method is used which furthermore distinguishes optically thin and thick clouds [5]. [6] introduced a two dimensional CSL, where the Red-to-Blue Ratio (RBR) values for every pixel are stored under consideration of the sun-pixel angle and pixel-zenith angle. For a cloudy pixel, the corresponding RBR values deviate from the CSL. Clouds can be detected by comparing these deviations with given thresholds. A major drawback of this two dimensional CSL is that the properties of a clear atmosphere differ significantly due to variations in atmospheric gases and aerosols. An iterative approach with a haze correction factor was introduced by [7]. There it is assumed that every pixel's RBR in the image is affected by the same factor due to the changes in the atmospheric conditions. We found that a single haze correction factor applied to the entire image is insufficient to account for the turbidity in the atmosphere. In order to test the applicability of a single correction factor, the ratio of two CSLs, corresponding to a Linke turbidity of 2 and 4 respectively, are created. The ratio does not show a uniform value across the CSL. Therefore, the four dimensional CSL approach used in this work links the RBR values for every pixel to the two angles but also additionally to the air mass and the DNI derived Linke turbidity. This approach makes the CSL cloud detection more robust under variable atmospheric conditions. Finally the image segmentation delivers all image pixel indexes that show a cloud.

Cloud Modelling Using Voxel Carving

The 3D cloud modeling is done by a voxel carving method [8], which allows to compute an object's 3D shape from multiple images taken from different viewpoints. Voxels are volume elements with a defined edge length in x , y and z dimension. The point of origin is located roughly in the center of the four camera positions. The voxels build a voxel space of finite size around the point of origin. The current system configuration uses a voxel space with an expansion of 27.6 km in x (easting) and y (northing) dimension and 10 km in z (height) dimension with a resolution of 50 m in all three dimensions. All four cameras are positioned inside the voxel space and their relative positions corresponding to the point of origin are known. Each camera pixel corresponds to a line of sight through the voxel space and beyond its borders. The main idea of the voxel carving method is to determine the cross sections of viewing cones from the four cameras to the border of image areas segmented as clouds (Fig. 1 (a to c)). Separate cloud objects are identified by examining the connection of all voxels that were identified as part of a cloud.

The omnidirectional cameras with their fisheye lenses are internally calibrated, using several images of a checkerboard pattern with known dimensions taken from different angles, following the procedure introduced in [9]. With the calibration, a scene point X_p with the perspective projection matrix P in homogeneous coordinates can be described by the pixel point u' in pixel coordinates with the projection equation.

$$P \cdot X_p = \lambda \cdot g(u'', v'') \cdot (A \cdot u' + t) \quad (1)$$

Estimates for A (stretch matrix) and t (translation vector) as well as the non-linear function $g(u'', v'')$, with u'' and v'' as the coordinates of the sensor plane, are generated by the calibration. λ describes the depth factor. With the calibration the 3D points of each voxel can be reprojected in the pixel coordinate, which in turn allows overlying the viewing cones from the four cameras inside the voxel space. The camera position is measured with GPS and its alignment is determined by an external calibration by tracking the moon during the night.

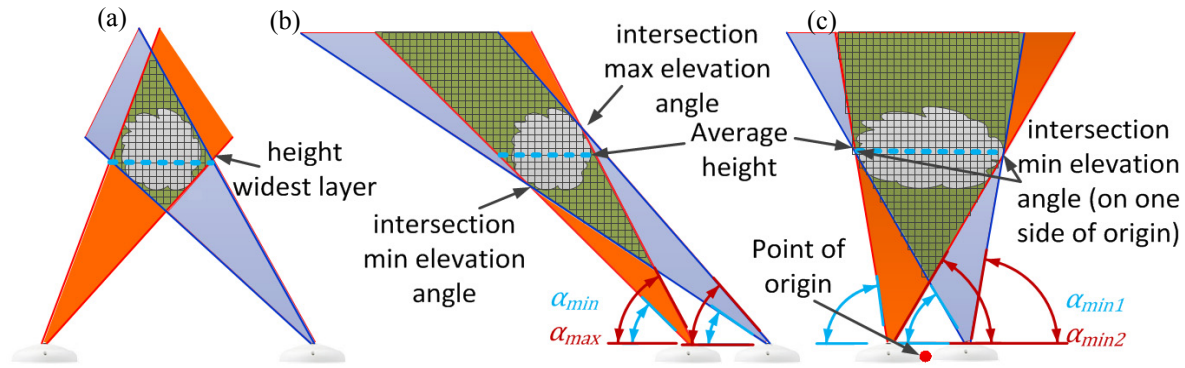


FIGURE 1. (a) 2D depiction of a small cloud inside the voxel space positioned at the center of the field of view of several cameras (widest voxel space layer corresponds to cloud height). (b) 2D depiction of cloud inside the voxel space positioned at the outskirts of the field of view of several cameras (intersection line of sight of several cameras at the cloud edges corresponds roughly to cloud height). (c) 2D depiction of large cloud inside the voxel space positioned at the center of the field of view of several cameras (intersection line of sight of several cameras at the cloud edges corresponds to cloud height)

In the following we will use the terms cloud object and cloud. A cloud object refers to the 3D cloud model inside the voxel space and cloud to the actual physical cloud. 3D cloud objects created by the first step of the voxel carving method result in most of the cases in over-dimensioned cone shaped objects. Without further adjustments of the cloud object shape, the cloud's size would be overestimated (green area in Fig. 1). The cloud objects can be categorized according to their size and the questions whether the cloud object is crossing one or more voxel space limits and whether the actual cloud is completely inside, partially inside or completely outside the voxel space. Depending on this classification, different methods are used to determine the cloud height. For small cloud objects which cross no limits of the voxel space the cloud center height can be assumed to be the widest horizontal voxel layer with the highest count of voxels (see Fig. 1 (a)). For most other types of cloud objects, the height can be determined by identifying the intersection of the camera field of views at the cloud edges. Looking at the 2D depiction of Fig. 1 (b), it can be seen that the cloud edges can be identified by the voxel with the corresponding minimum and maximum pixel elevation angle ($\alpha_{min/max}$) of a cloud objects cross section. In the case that a large cloud is partially above the point of origin, the intersection of the camera field of views at the cloud edges are defined by the minimum pixel elevation angles on both sides of the point of origin (Fig. 1 (c)). Figure 2 illustrates a cloud object before the height is derived (yellow object). In order to create a cross section of this cloud object as depicted in Fig. 1 the main direction of the cloud object has to be identified. For this purpose a 2D projection of the cloud object in the x and y plane is created. The main direction can be described by a polynomial function of first degree between the point of origin and the average coordinates of the 2D projection. A main plain, which cuts through the cloud object (Fig. 2 plane in green), can be derived from the main direction. The voxel which are on the plane describe the desired cross section.

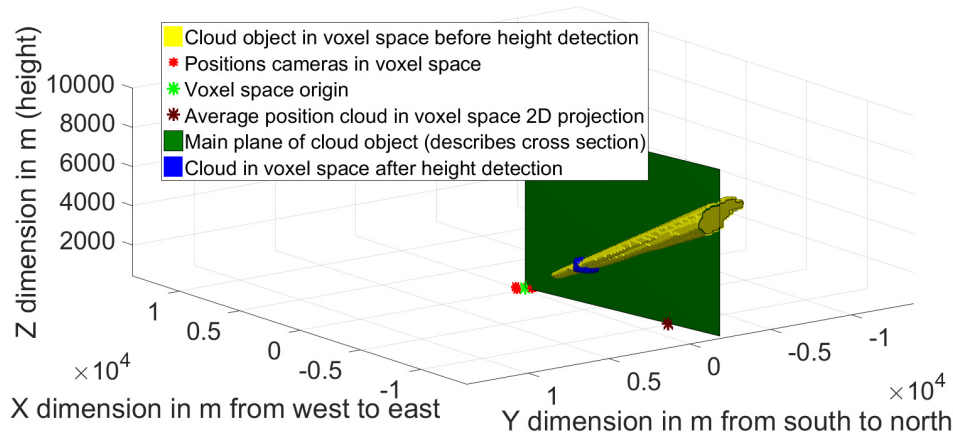


FIGURE 2. Voxel space with example cloud in yellow before height detection and in blue after height detection

The voxels which belong to the cross section can be reprojected in the four camera pixel coordinates. Thus, all corresponding camera pixel elevation and azimuth angles are known. Vector coordinates from the cameras to the cloud edges can be calculated by the functions:

$$x_{\max/\min} = r \cdot \sin(90 - \alpha_{\max/\min}) \cdot \cos(\varphi) \quad (2)$$

$$y_{\max/\min} = r \cdot \sin(90 - \alpha_{\max/\min}) \cdot \sin(\varphi) \quad (3)$$

$$z_{\max/\min} = r \cdot \cos(90 - \alpha_{\max/\min}) \quad (4)$$

with the maximum or minimum camera pixel elevation angle $\alpha_{\max/\min}$, the corresponding camera pixel azimuth angle φ and the radius r , which describes the distance between the camera and the vector coordinates. The length of the radius r is increased until the intersection points between the lines of sights of the four cameras to the cloud edges are detected. With four cameras, a total of six intersection points for each cloud edge exist. The actual cloud height is calculated as the average z coordinate of all intersection points for both cloud cross section edges. A geometrical cloud thickness and thus an upper and lower height limit is estimated as function of the absolute cloud height (decreasing thickness with increasing absolute height). The resulting cloud object after the height detection is shown in Fig. 2 (blue object).

For clouds which are partially outside the voxel space, only the cloud edge inside the voxel space is used for the height detection. This approach results in increased uncertainties for very large clouds which exceed all four vertical voxel space borders, for clouds which are completely outside the voxel space or for clouds with increased segmentation or modelling errors (especially clouds at the camera horizon). The first case usually describes an overcast situation where the cloud height detection is not from utmost interest. For the second and the third case, a further processing step is added to avoid large errors. These two cases can be identified by an increased relative standard deviation (rsd) between the various intersection positions in the z dimension of the camera field of views at the cloud edges. Cloud heights, which are detected with a low rsd ($< 5\%$) are stored in a database with their time stamp and an expiration date (max 8 hours). All very large clouds or clouds with a high rsd ($> 15\%$) are given a cloud height from the data based preprocessed using a Kalman filter. A prediction is generated from a data series which in general is more robust than a single measurement by itself. A new prediction is generated for each new measurement under consideration of the previous prediction. The influence of the previous prediction and the current measurement on the next prediction depends significantly on the measurement noise. Figure 3 illustrates the complete voxel space from the example with cloud objects after the height detection.

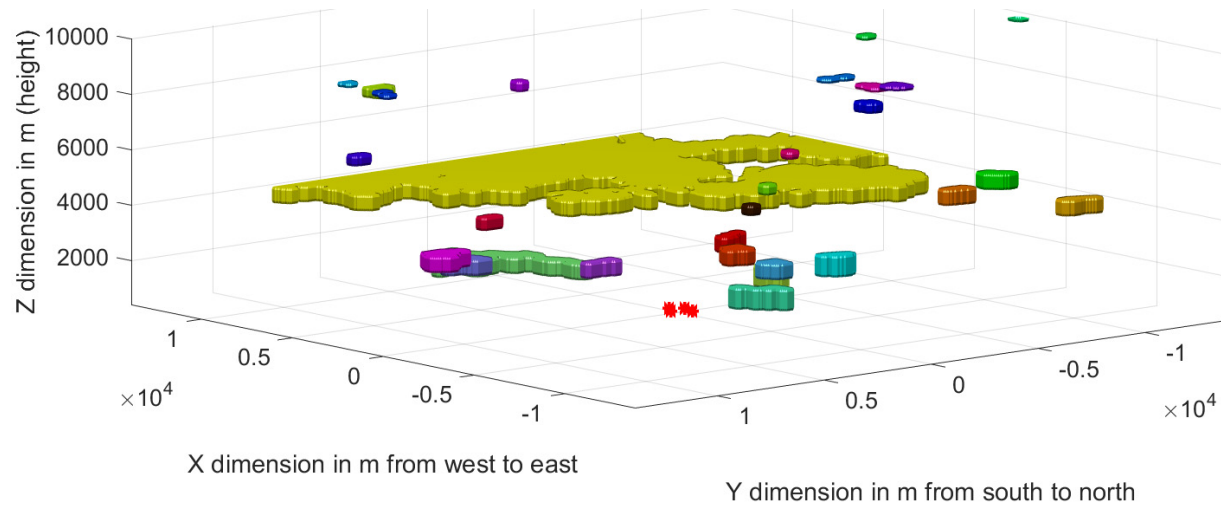


FIGURE 3. Voxel space with various cloud objects after height detection

Cloud Tracking

Cloud objects of the current image series are compared directly with cloud objects of the previous image series (see Fig. 4 (a) & (b)). For each cloud object of both image series a 2D projection is created (see Fig. 4 (c) & (d)). The 2D projection corresponds to the centre layer of the cloud defined during the cloud height detection. A cross

correlation algorithm is used for the cloud object comparison. Cloud projections with the highest correlation coefficient are allocated to each other. During a plausibility check, cloud allocations are assessed. Matches with cloud objects which appear to change their altitude or result in a theoretical speed beyond a certain threshold are rejected. Cloud objects without a suitable allocation are assumed to have left the voxel space or they are introduced as a new independent cloud object, depending on whether the cloud object result from the previous or current image set.

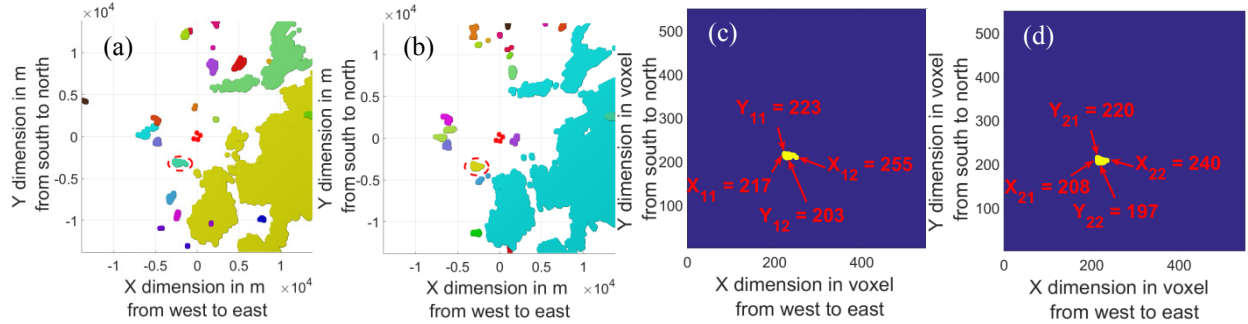


FIGURE 4. (a) Voxel space top view with cloud objects from previous image series (example cloud object marked), (b) Voxel space top view with cloud objects from current image series (example cloud object marked), (c) 2D cross section of example cloud from previous image series, (d) 2D cross section of example from current image series

Motion vectors are calculated for clouds with sufficient historical information from previous images. Spatial displacements are detected by comparing the position of the 2D cloud projection edges in both axes. Cloud segmentation errors and thus cloud 3D modelling errors as well as cloud height detection errors increase towards the horizon. Small pixel errors can have a big impact depending on the actual height of the cloud. This complicates the cloud matching and subsequent determination of the motion vector for such clouds. Therefore, only clouds which are positioned in an inner part of the voxel space are considered for the determination of motion vectors (see Fig. 5 (a)). Figure 5 b illustrates an ASI image with some exemplary highlighted clouds, which are positioned inside or outside the inner voxel space. Clouds outside of the inner voxel space or clouds from the inner voxel space without historical information get a motion vector allocated from a database. Valid motion vectors are stored into a database with their corresponding cloud height. Every entry of the database is equipped with an expiration date of 8 hours. For each cloud without valid motion vector an individual excerpt of the database is taken by considering the target cloud height. A new motion vector in x and y dimension is generated by applying a Kalman filter on the database excerpt (as described for the cloud height).

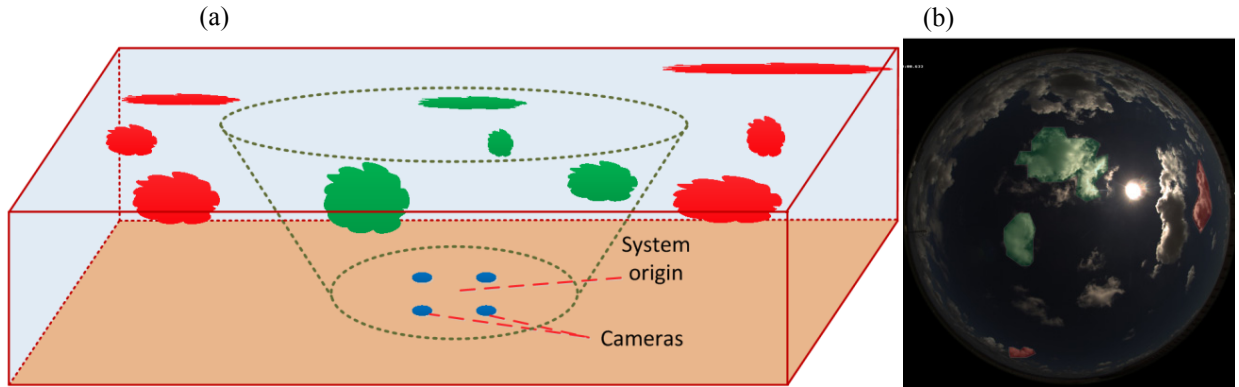


FIGURE 5. (a) Illustration of inner (dotted green line) and outer (continuous red line) voxel space. Only clouds of the inner voxel space (green clouds) are used for the determination of the motion vectors. Red clouds with higher segmentation and modelling errors get motion vectors allocated. (b) ASI sky image with exemplary clouds marked green for the inner voxel space and red for the outer voxel space

For the forecast, the processed cloud objects are displaced individually according to the allocated motion vectors in x and y dimension. Predictions for the cloud positions are made for lead times up to 15 minutes ahead. Due to the acceptable computation time of 30 s (time between two image series), the voxel space is currently limited to a

maximum size of 27.6 km x 27.6 km x 10 km with a resolution of 50 m (voxel edge length). It might happen that for some lead times all relevant clouds have left the voxel space, which would lead to clear sky predictions. This is mainly a problem during low sun elevation angles, with fast moving clouds and for predictions which look farthest into the future. This issue is tackled by assuming a persistent cloud pattern for the small space under observation and the short time window with a maximum lead time of 15 minutes. All voxels which leave the voxel space at one side will reappear on the opposite side.

Creation of Irradiance Maps

Creation of the spatially resolved DNI maps requires the cloud shadow projection, the calculation of the current clear sky DNI and determination and allocation of transmittance values to the cloud objects. At first, a topographical model is created for a grid of GPS coordinates. The shadow projection on the topographical model is determined via a raytracing approach [10]. A binary shadow map is created for each cloud object individually. For this purpose a vector in direction of the sun is created for each voxel identified as cloud. These vectors are turned at their base point by 180° and projected to the topographical model. All pixels of the topographical model hit by one of these vectors are considered as shaded.

For the determination of the clear sky DNI, the Linke turbidity is calculated from DNI measurements according to [11]. Shaded Linke turbidity measurements are sorted out using the method from [12, 13]. The current Linke turbidity is calculated by the time-weighted recent and unshaded Linke turbidity measurements. For the current and future time stamps a clear sky DNI is calculated with the current Linke turbidity according to [11].

The transmittance τ of clouds which directly shade a ground based DNI measurement station is measured as quotient of the shaded and clear sky DNI.

$$\tau = DNI_{shaded} / DNI_{clear} \quad (5)$$

Recent clouds in similar heights are assumed to have similar optical properties for the time periods under consideration. Transmittance measurements are divided by thresholds in a thin and thick cloud class. All clouds without a transmittance measurement are also classified in thin and thick clouds depending on their cloud height and receive an appropriate time weighted average transmittance derived from the previously classified transmittance measurements.

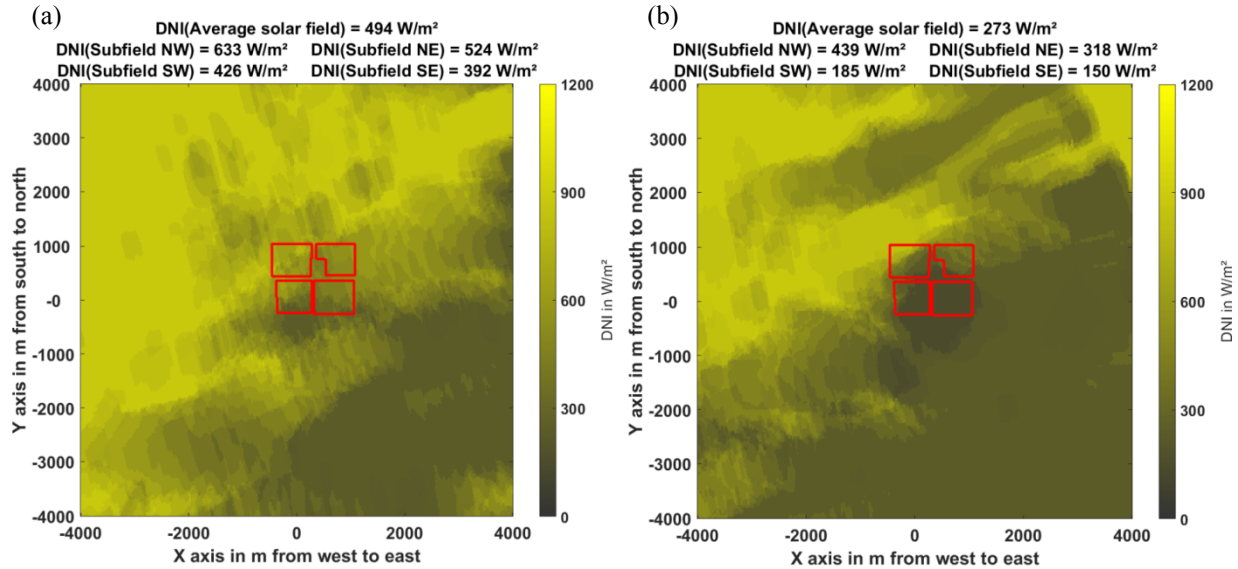


FIGURE 6. (a) DNI map lead time 0 (b) corresponding DNI map lead time 10 minutes

Detailed spatially resolved DNI maps are created by combining the topographical model with the shadow projections, transmittance measurements and clear sky DNI for the current and predicted time. Errors are reduced by merging various current and historical DNI maps to temporal averaged DNI maps. Instantaneous DNI values are of minor interest for CSP plants with their thermal inertia. Figure 6 illustrates DNI maps with an edge length of 8 km, a

spatial resolution of 400 m² and a temporal average of 5 minutes. Figure 6 (a) shows a DNI map with a lead time of 0 minutes and Fig. 6 (b) the corresponding DNI map with a lead time of 10 minutes. The red frames indicate the subfields of the La Africana parabolic through power plant. The DNI map headers indicate the average DNI for the subfields and for the entire solar field

VALIDATION OF DNI MAPS

For the validation of the DNI maps the extensive measurement system of the PSA is used. Especially worth mentioning is a unique shadow camera system [14], which allows the validation of spatially resolved maps (singular irradiance measurements as conducted by pyrheliometers do not provide spatially resolved irradiance information). Furthermore, a network of pyrheliometers and pyranometers as well as a ceilometer are used for detailed validations. The validation results of a 30 days period are presented in detail in [15]. Here, only a summary of the most relevant results are presented. The mean absolute error (MAE) and the relative MAE are defined by

$$MAE = 1/N \cdot \sum_{i=1}^N |p_i - o_i| \quad (6)$$

$$relMAE = 100\% / \bar{o} \cdot MAE \quad (7)$$

with p_i as predicted DNI, o_i as the observed reference DNI, \bar{o} as the average observed reference DNI and N as the total number of measurements. Figure 7 (a) shows the MAE and relMAE derived from three ground based pyrheliometer measurements compared to the corresponding pixel in the DNI map for 30 days. For a lead time of 7.5 minutes and a 15 minute temporal average, a relative MAE of 15 % is observed. Fig. 7 (b) shows the comparison to the shadow camera system for field sizes between 25 m² and 4 km², lead times between 0 min and 15 min and 1 min temporal averages for one example day. Spatial aggregation effects, present in industrial size solar power plants, reduce the deviations significantly. A typical field of a 50 MWe parabolic through power plant in southern Spain has an edge length around 1400 m (ca. 2 km²) which corresponds to an MAE around 14.8 % for a lead time of 15 minutes (further decrease of deviations for larger solar fields).

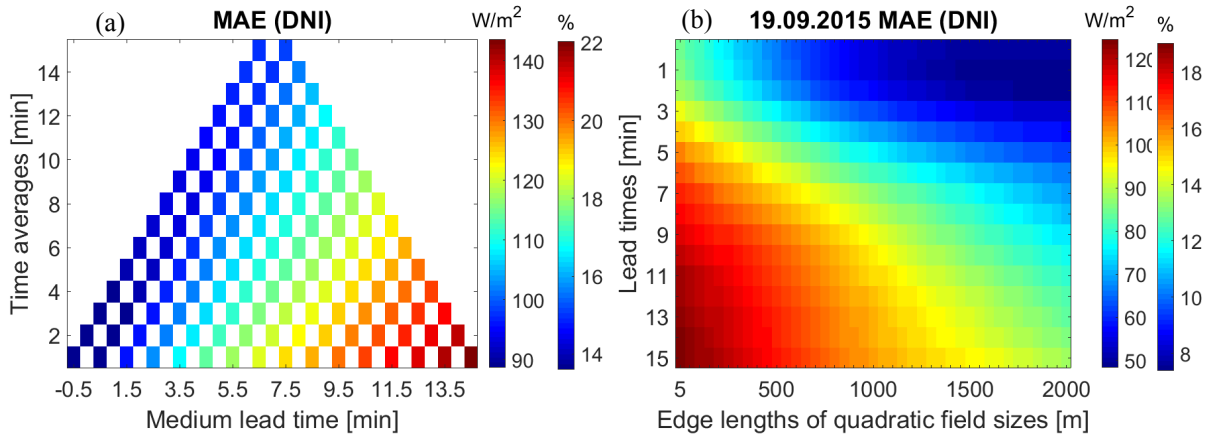


FIGURE 7. (a) MAE derived from three ground measurements stations in comparison to the corresponding pixels in the nowcasted irradiance maps on 30 days (b) MAE in comparison to the shadow camera system for field sizes between 25 m² and 4 km², lead times between 0 min and 15 min and 1 min temporal averages for one day

CONCLUSION

A novel nowcasting system with sub minute temporal resolution based on four standard surveillance cameras has been developed and validated. Spatially resolved DNI maps with an edge length of 8 km and a resolution of 25 to 400 m² are produced in real time for lead times up to 15 minutes. All hardware components were chosen for a quick and modular installation with optional wireless LAN data transmission and PV power supply. The system uses an enhanced four dimensional clear sky library and cloud segmentation approach, which is robust under variable atmospheric conditions. 3D cloud objects are created by the voxel carving method. The cloud heights are detected via reprojection of the cloud object's cross sections into the camera images, by which the corresponding pixel azimuth and elevation angles of the cloud edges are identified. The cloud height itself is located at the intersection

from camera pixel sight vectors corresponding to the identified cloud edges. Apart from the cloud height, each cloud object is associated with distinct geometrical and optical attributes (height, position, surface area, volume, transmittance, etc.). A newly developed individual cloud tracking approach of the 3D cloud objects inside the voxel space is applied. Therefore, the system can handle complex but frequent multilayer cloud conditions. A comprehensive validation campaign on 30 days with various weather conditions was conducted at the PSA. The influences of temporal and spatial aggregation on the prediction quality with particular relevance for industrial size solar power plants, were analyzed. The extensive validation and the demonstration of the system in the commercial La Africana power plant prove its applicability for solar plants.

ACKNOWLEDGEMENT

The work presented in this publication has received funding from the German Federal Ministry for Economic Affairs and Energy within the WobaS project, which enabled the development of the WobaS nowcasting system and the shadow camera system. The European Union's Horizon 2020 programme (PreFlexMS, Grant Agreement no. 654984) financed partially the initial development of the shadow camera system. The operation of the all-sky imagers and other ground measurements was partly financed by the European Union's FP7 programme under the Grant Agreement no. 608623 (DNICast project).

REFERENCES

1. Huang H. et al., Correlation and local feature based cloud motion estimation. Proceedings of the Twelfth International Workshop on Multimedia Data Mining. ACM, pp. 1-9, (2012)., doi: 10.1145/2343862.2343863
2. Chow C.W. et al., Cloud motion and stability estimation for intra-hour solar forecasting, [Solar Energy](#) 115, pp. 645-655, (2015)., doi: 10.1016/j.solener.2015.03.030
3. Zhenzhou Peng et al., 3D cloud detection and tracking system for solar forecast using multiple sky imagers, [Solar Energy](#) 118, pp. 496-519, (2015)., doi: 10.1016/j.solener.2015.05.037
4. Blanc P. et al., Short-Term Forecasting of High Resolution Local DNI Maps with Multiple Fish-Eye Cameras in Stereoscopic Mode, [AIP conference Proceedings](#) 1850, (2017)., doi: 10.1063/1.4984512
5. Wilbert S. et al., Application of whole sky imagers for data selection for radiometer calibration, 32nd European Photovoltaic Solar Energy Conference and Exhibition, pp. 1493-1498, (2016)., doi: 10.4229/EUPVSEC20162016-5AO.8.6
6. Chow C.W. et al., Intra-hour forecasting with a total sky imager at the UC San Diego solar energy testbed, [Solar Energy](#) 85, pp. 2881-2893, (2011)., doi: 10.1016/j.solener.2011.08.025
7. Ghonima M. S. et al., A method for cloud detection and opacity classification based on ground based sky imagery, In: [Atmospheric Measurement Techniques](#) 5.11, pp. 2881-2892, (2012)., doi: 10.5194/amt-5-2881-2012
8. Kutulakos K. et al., A Theory of shape by Space Carving, [International Journal of Computer Vision](#) 38, pp. 199-218, (2000)., doi: 10.1023/A:1008191222954
9. Scaramuzza D. et al., A Toolbox for Easily Calibrating Omnidirectional Cameras, IEEE International Conference on Intelligent Robots and Systems, pp. 1493-1498, (2006)., doi: 10.1109/IROS.2006.282372
10. Oberländer D., et al., Cloud shadow maps from whole sky imagers and voxel carving, ICIM, Boulder, (2015).
11. Ineichen P. and R. Perez, A new airmass independent formulation for the Linke turbidity coefficient. [Solar Energy](#) 73, pp. 151-157, (2002)., doi: 10.1016/S0038-092X(02)00045-2
12. Hanrieder N. et al., Modeling beam attenuation in solar tower plants using common DNI measurements. [Solar Energy](#) 129, pp. 244-255, (2016)., doi: 10.1016/j.solener.2016.01.051
13. Wilbert S. et al., Uncertainty of rotating shadowband irradiometers and Si-pyranometers including the spectral irradiance error. [AIP Conference Proceedings](#) 1734, (2016)., doi: 10.1063/1.4949241
14. Kuhn P. et al., Shadow camera system for the generation of solar irradiance maps. [Solar Energy](#) 157, pp. 157-170, (2017)., doi: 10.1016/j.solener.2017.05.074
15. Kuhn P. et al., Validation of an all-sky imager based nowcasting system for industrial PV plants, [Prog Photovolt Res Appl.](#), pp. 1-14, (2017)., doi: 10.1002/pip.2968